Severe Storm Latent Heat Release: Comparison of Radar Estimate Versus a Numerical Experiment

DHIRENDRA N. SIKDAR, ROBERT E. SCHLESINGER, AND CHARLES E. ANDERSON

Department of Meteorology, and Space Science and Engineering Center, The University of Wisconsin, Madison, Wis. 53706

(Manuscript received 9 November 1973, in revised form 19 March 1974)

ABSTRACT

The time variation of mass-integrated liquid water and latent heat release for a severe thunderstorm in marked vertical wind shear is investigated for an actual Oklahoma storm and for a two-dimensional numerical modeling experiment.

For the actual storm, an approximate continuity equation for liquid water variation is used together with profiles of radar reflectivity. Empirical relationships are utilized to determine the rainfall rate (flux) and liquid water content from the radar reflectivity profiles. Estimates of total storm water mass are obtained from the reflectivity profiles for the volume swept by the radar beam in the vertical. The downdraft evaporation rate is parameterized on the basis of a previous study which estimated this quantity as a residual in the continuity equation for liquid water mass.

To estimate latent heat release and total liquid water mass from the numerical model, the two-dimensional cloud is extended to a three-dimensional region whose horizontal cross sections are ellipses approximating typical observed PPI radar echo shapes. At each level, horizontal averages of relevant integrands are assumed equal to those in the model plane.

It is found on the basis of these analyses that at maturity, the actual storm and the model storm exhibit comparable magnitudes with respect to both latent heat release and liquid water content.

1. Introduction

The water vapor and energy budgets of severe storms have been of interest since even before the Thunderstorm Project (Byers and Braham, 1949). Braham (1952), utilizing the Project data, attempted to evaluate various components of thunderstorm energetics and found latent heat release to be the major one. However, the Ohio storms investigated in the Project were of air-mass-type and relatively short-lived. Some large, mature hailstorms exhibit a quasi-steady state lasting for a few hours, possibly as a single "supercell," and process much more water vapor than an ordinary thunderstorm. The latent heat release in an ordinary storm is about 5×10^{11} cal sec^{-1} (Braham, 1952) while in a severe storm it may be in excess of 8×10^{12} cal sec^{-1} (McLaughlin, 1967), an order of magnitude higher.

While various investigators have studied severe storm energetics at a particular time and place, very little progress has been made in regard to knowledge of their time variations because of the hazards and difficulties involved in frequent sampling of the interior of the storm by aircraft sensors. In recent years, however, remote sensing of the water budget in severe storms has been made possible by calibrated weather radars utilizing relationships between the cloud liquid water content and the radar reflectivity profiles as a function of time. The time lapse echo contour displays in CAPPI (Constant Altitude Plan Position Indicator) mode essentially provide such information. Using such a concept, Barge (1968) estimated the latent heat released during each of four severe storms near Montreal and found that the energy output ranged from one to three orders of magnitude higher than for a moderate storm.

The purpose of this paper is twofold: first, to find out the nature of the time-varying liquid water mass and latent heat release of a typical severe storm as deduced from radar data; second, to compare these observed magnitudes with those obtained from a two-dimensional numerical model simulation experiment.

2. An approximate scheme for computing from observed data

One can visualize a severe storm as consisting of two regions: a core where air is ascending or descending without mixing (no entrainment), and a shell of cloud debris with little vertical air motion. The primary source of water vapor for a storm is the inflow of moist air through the cloud base. A part of the condensed water vapor is stored in the core and is evaporated later in the downdraft; a second part evaporates in the shell, due to horizontal advection of dry air into the storm, and a third part is transformed from cloud droplets to raindrops or

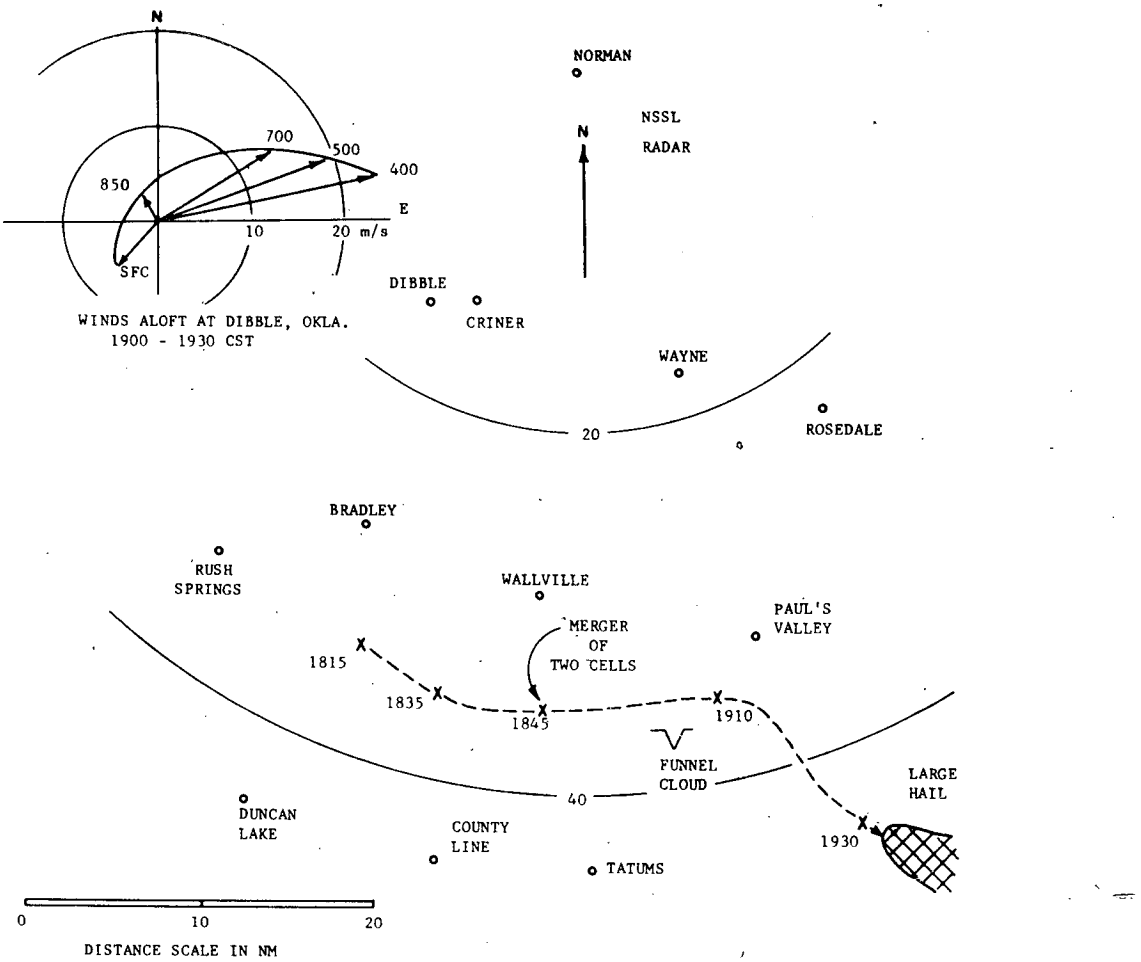

FIG. 1. Storm track as viewed from the NSSL radar.

hailstones and falls out. A weather radar is capable of detecting these changes in terms of total precipitation mass as the storm evolves. However, some condensate may not attain radar-detectable size, may be stored as cloud droplets, or may escape as ice crystals through the top of the storm so that latent heat release computed from radar data will be an underestimate.

In computing the time variations of latent heat release from the radar reflectivity profiles the following basic steps are involved:

1) To establish a reflectivity-surface rainfall relationship,

2) To establish a reflectivity-liquid water content relationship,

3) To solve a continuity equation for radar-detectable liquid water content on the basis of steps 1 and 2.

It should be pointed out here that the volume sampled by the radar beam is less than the total volume of the storm, and therefore the estimate of liquid water content is less than actual; however, since we are mostly concerned with the time variation of the liquid water content and not in the absolute magnitude, our estimates of the generation term in the liquid water continuity equation should be correct at least within a factor of 10.

3. Data source and analysis technique

Radar and rainfall data were obtained from the National Severe Storms Laboratory (NSSL), which has a 10-cm WSR-57 radar at Norman, Okla., with a peak transmission power of 0.5 MW and a 2° conical beamwidth. The PPI photographs obtained from it show reflectivities at intervals of 10 dB with ±3-dB calibration accuracy. Supplementing this is an MPS-4 RHI radar (1.4° conical beam) calibrated to read reflectivities at 10-dBZ intervals, depicting the vertical distribution of liquid water. Radar reflectivity contours were not range-normalized and are relative contours. Only single azimuth RHI displays, scanning through the storm core, were available for computing liquid water mass at each time. Thus, as noted above, the calculated water content will be less than that in the total storm volume.

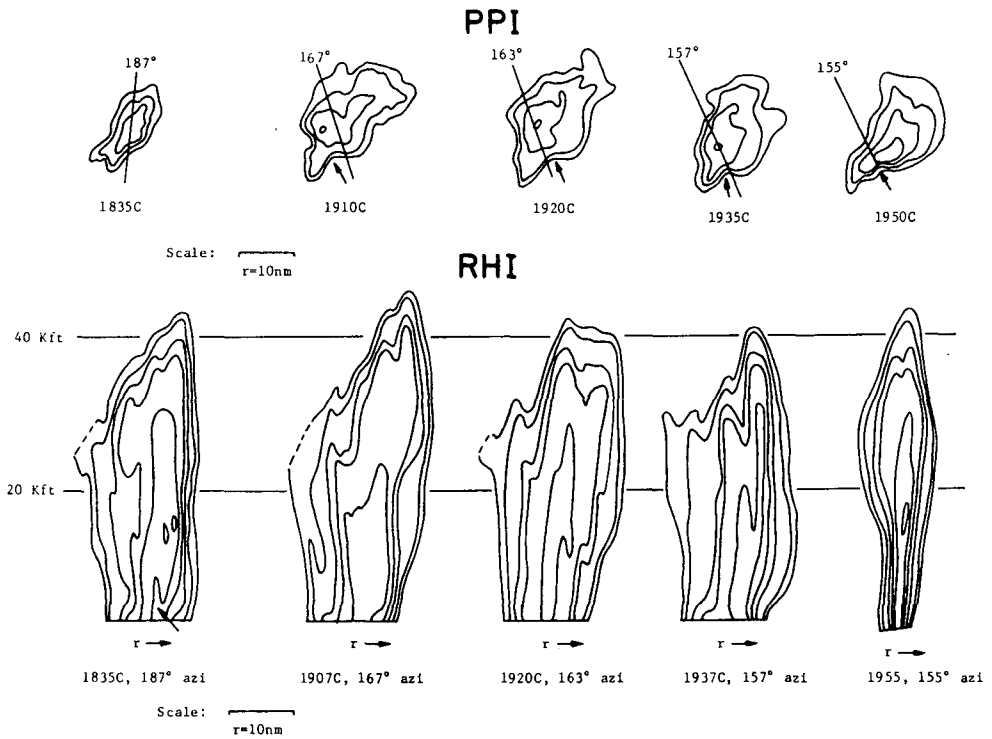

FIG. 2. A sample of PPI (elevation 2°) and RHI reflectivity profiles of the storm investigated. Reflectivity values are in steps of 10 dBZ, increasing towards the storm center with the outermost one representing 20 dBZ.

A surface meso-network covering approximately 5500 mi^2 provides all standard meteorological parameters (Barnes *et al.*, 1971).

a. Some features of the selected storm

The 1200 GMT chart on 24 May 1968 indicated a weak quasi-stationary front oriented NE-SW across central Oklahoma; at 500 mb a long-wave trough was present in the western Rockies with southwesterly flow over Oklahoma. The movement of a short-wave trough into Oklahoma from the Texas panhandle and an incursion of warm moist air from the Gulf of Mexico (dewpoint temperature about 69F) at lower levels were conducive to explosive development of a few convective cells by late afternoon.

A strong convective cell intensified rapidly by 1900 CST to the southwest of the existing cells in the southeastern portion of the NSSL meso-network. Severe weather reports in *Storm Data* included a funnel cloud southwest of Paul's Valley at 1910 CST along with $\frac{3}{4}$ to $1\frac{1}{2}$-in hail from 1936 to 2000, between Wynnewood and Davis, Okla. (U. S. Dept. of Commerce, 1968). The storm trajectory through the surface meso-network is shown in Fig. 1. The hodograph shown in the inset indicates pronounced wind shear in the vertical and the storm appears to have been moved to the right of the upper winds. The PPI and RHI histories of the storm are shown in Fig. 2. The area of the storm increased significantly around 1845 CST. An indentation (see arrow) to the south of the storm became very pronounced between 1900 and 1930 on the PPI, indicating a probable location of the weak echo region (Marwitz, 1972). On the RHI time section, this strong updraft region appeared as a notch in the southeast sector of the storm (see arrow). The smaller number of contours in the PPI display may be attributed to underestimation of reflectivity near the storm center by the radar, as contours in both the RHI and PPI plots are at 10-dBZ intervals.

b. Rainfall analysis and radar reflectivity profiles

Of the various water sources and sinks, only the rainfall can be measured with any reasonable degree of accuracy. Accordingly, the radar reflectivity profiles were first calibrated against the rainfall rates obtained from the meso-network. The rainfall rates R (mm hr^{-1}) were computed directly from the recording raingauge strip charts and the reflectivity Z over the raingauges at the same time from the radar photographs. The relationship obtained for 23–24 May 1968 using 85 data pairs was $Z=1.5\,R^{1.96}$. For details the reader is referred to Ellrod (1973).

Fig. 3 presents the time variations of the integrated rain flux over the surface rain area during the life cycle of the severe storm under study. This parameter varied from 7×10^5 to slightly more than 4×10^6 kg sec^{-1}, in reasonable agreement with values obtained for severe

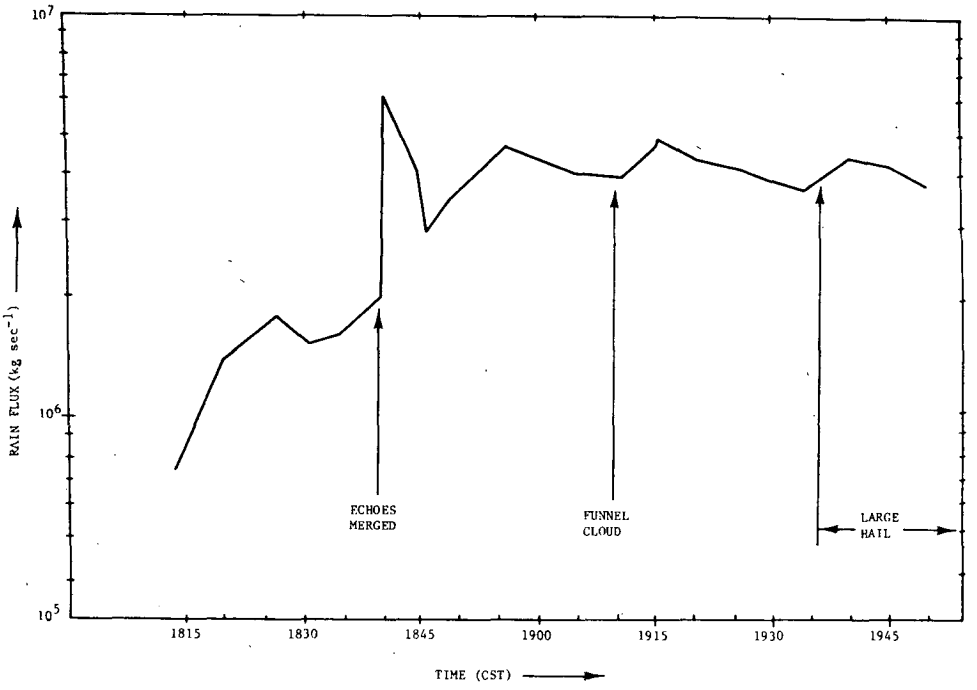

FIG. 3. Time variation of rain flux estimated from radar reflectivity data.

storms (Geotis, 1971; Fankhauser, 1971; McLaughlin, 1967) using Z-R relationships. Four prominent peaks separated by 15 to 25 min are apparent in this diagram. Funnel clouds were reported 15 min after the second maximum, while the large hail started 20 min after the third maximum.

c. *Radar reflectivity profiles and liquid water content*

In radar studies of storms, the PPI observations are taken more frequently than RHI (range height indicator) observations. Unfortunately, in this case study, some problems with the signal integrator of the PPI radar system resulted in underestimates of radar reflectivity values (Wilson, 1963), so that RHI data had to be used. The MPS-4 radar tracked the storm as a function of time and sampled a slice of the storm through the center at nearly regular intervals.

In computing the liquid water content from radar reflectivity profiles, the volume of each inner shell bounded by two reflectivity contours swept along the radar beam in the vertical is determined treating each shell as a small angular sector of a cylinder (Fig. 4). Note that the axis of all approximating cylinders intercepted by the radar beam is at the radar site. The shell volumes (for 5 shells in steps of 10 dBZ) so obtained are first multiplied by representative liquid water content derived from the Gunn and Marshall (1958)[1] equation, and then added to yield the volume integrated liquid water mass along a particular azimuth. This approach implicitly assumes a constant distribution of ΣND^6 with height where N is the drop concentration, D is the diameter of the water droplets and the summation extends over the droplet size spectrum in a unit volume. To further simplify the model, all water content is assumed to be in liquid form regardless of altitude.

It should be re-emphasized here that the total water mass estimated from this method will be less than what would be expected for the total volume of the storm. However, since most of the water vapor is processed through the storm core, the time changes should not be greatly underestimated and should show little dependence upon the shape of horizontal storm sections as long as the RHI scan is through the storm core rather than the peripheral regions.

The total radar-detectable liquid water mass thus derived is presented in Fig. 5. The total liquid water mass, as one would expect, increased rapidly during the early stages of the storm, reaching a maximum of 5.7×10^8 kg around 1920 CST. This is at least one order of magnitude higher than estimates provided by Braham (1952) for a moderate thunderstorm, as might be expected since severe "supercell" storms are generally more voluminous than the air-mass storms studied by Braham, as well as more intense.

4. Water and energy budgets of the storm

The rate of condensation in the storm has been computed from a continuity equation for radar-detectable

[1] Gunn-Marshall (1958) equation: $Z=2.39\times10^4\ M^{1.82}$ where Z = radar reflectivity (mm^6 m^{-3}), and M = liquid water concentration (gm m^{-3}).

liquid water mass similar to one used by Holtz (1968):

$$\frac{dW}{dt}=G-R-E \tag{1}$$

where W is the total radar-detectable liquid water mass, G the condensation rate in the updraft, R the rainfall rate, and E the evaporation rate in the downdraft.

The term dW/dt can be directly obtained by finite differences from Fig. 5, while the rainfall rate R is obtained from direct measurements properly weighted for a horizontal area swept by the radar beam. A problem arises with the estimation of E, as this component is not measured at all. However, previous investigators (Braham, 1952; McLaughlin, 1967), deriving this term as a residual in their water balance equations, have found it to be of the same order of magnitude as R. In his analysis of a severe storm in Oklahoma, the area involved in this study, McLaughlin found that the evaporation rate at peak storm intensity was two-thirds the rainfall rate. Accordingly, this approximation has been used here for the duration of the storm in order to simplify the budget equation (1), although this simplification should not be construed as generally valid for all storms, in view of widely varying rainfall efficiency from case to case.

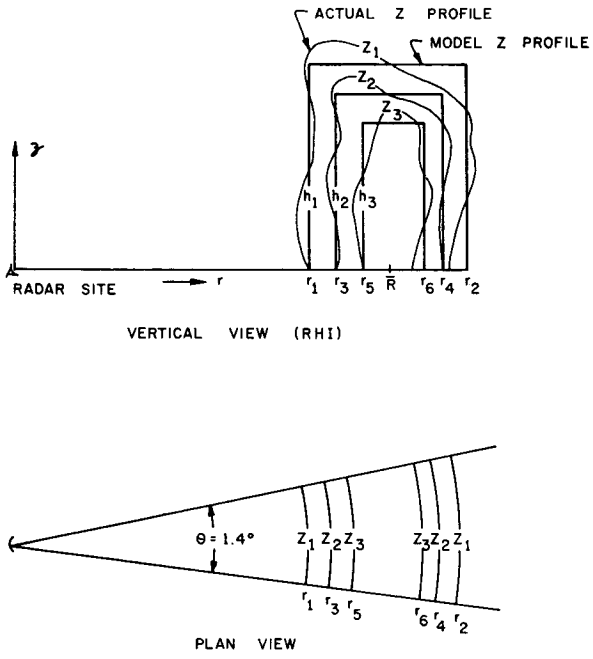

FIG. 4. A schematic diagram depicting the estimation of volumes between successive reflectivity contours within the radar beam width.

Volume of the shell between two reflectivity contours

$$=\bar{R}\theta[(r_2-r_1)h_1-(r_4-r_3)h_2]$$

where r denotes radial distances of the contour;
h denotes approximated height of the model Z profile;
$\bar{R}$ is the arithmetic mean, $(r_1+r_2)/2$, used to compute beam width at the midpoint of the shell;
θ is the radar beam width.

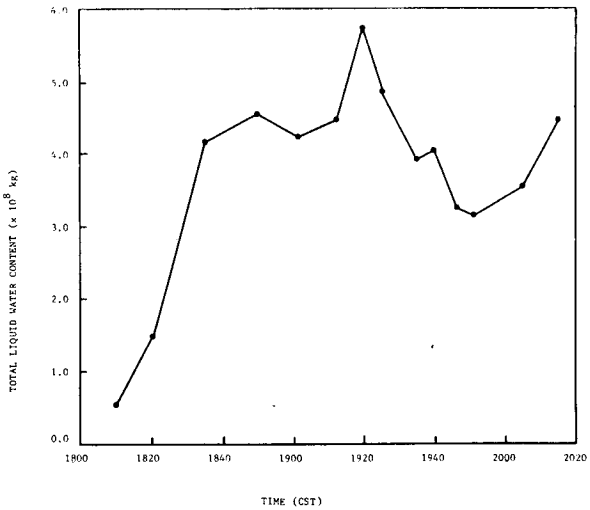

FIG. 5. Time variation of total liquid water content as derived from the RHI profiles.

The resulting condensation rate thus obtained showed a few peaks with the highest one (8×10^6 kg sec^{-1}) near 1915 CST, about 20 min before the onset of large hailfall from the storm was reported. The peak of 6.7×10^6 kg sec^{-1} around 1840 CST may be attributed to the merging of the storm with an adjacent cell (not shown). The other peaks in the fluctuation of storm energetics, e.g., at 1825 CST and 1945 CST, are likely due to re-intensification of the existing "supercell" storm.

The condensation rate G when multiplied by the heat of vaporization at 0°C (597 cal gm^{-1}) yields the equivalent heat release plotted in Fig. 6. A maximum value of nearly 4.7×10^{12} cal sec^{-1} (equivalent to 1.7×10^7 MW) is obtained. This is more than an order of magnitude higher than for a moderate thunderstorm (Braham, 1952) and in general agreement with values obtained by other investigators (McLaughlin, 1967; Brown, 1967; Geotis, 1971; Sikdar *et al.*, 1970). Thus we may safely assume that our subject storm is typical of severe storms in respect to the magnitude of energy release and its time variability.

5. A comparison between observations and the numerical model

a. Some main features of the model

In a theoretical study of the joint influence of low-level moisture supply and mid-tropospheric ambient wind shear upon the intensity and persistence of mature cumulonimbus (Schlesinger, 1973), a two-dimensional anelastic numerical model was previously used for a series of comparative experiments. Details of the governing equations, initial and boundary conditions are presented in the above reference. Although updraft intensity was reduced by shear, it was found that moder-

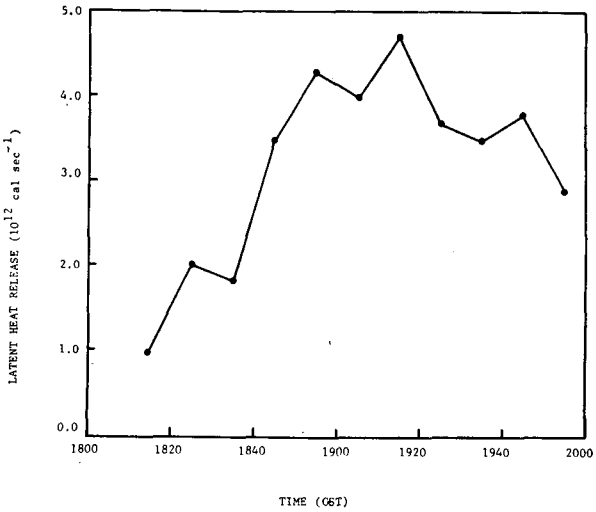

FIG. 6. Time variation of latent heat release.

ate shear supported a relatively persistent storm whose configuration considerably resembled patterns inferred observationally for large "supercell" storms. The model storm used in the current study exhibited a single dominant front-fed updraft whose intensity and vertical profile did not change greatly for over 30 min; the main rainfall occurred toward the upshear side, where a cold downdraft developed at middle and lower levels.

The initial base-state profiles of temperature and relative humidity used in the previous comparative experiments are shown in Fig. 7, and the horizontal wind profiles in Fig. 8. Note that the reproduction of any one specific storm situation was not intended. Rather, the assumption of a shallow moist layer surmounted by a deep dry layer as shown in Fig. 7 was based on mean climatological soundings associated with severe hailstorms in the southern Great Plains (Fawbush and Miller, 1953). The shallow upper stable layer is included to avoid excessive interaction of convection with the rigid top boundary.

Each comparative experiment simulated 80 min of time, and showed an updraft peak at 30 to 35 min. Within the range of initial environments shown, two moderate-shear cases (M1 and M2) and the very moist strong-shear case (H3) exhibited updrafts whose vertical profiles and intensities showed only slight change with time from 40 through 70 min. In this sense, these storms more nearly approximated a quasi-steady mature stage than the other cases. Such quasi-steady behavior has previously been inferred observationally for some persistent large middle-latitude storms in environments with marked shear (Browning and Ludlam, 1962; Browning and Donaldson, 1963; Fankhauser, 1971). Also, as seen in Fig. 9, case M2 at maturity exhibits considerable resemblance to the structure inferred for such "supercell" storms by Ludlam (1963):

1) Relative to the storm motion, which is from left to right and in the downshear direction, the main updraft is fed from downshear at low levels, and tilts upshear at least up to middle levels.

2) Upshear of the updraft, a downdraft is fed by dry middle-level air from behind the storm, although this air enters the storm from lower levels than suggested by Ludlam.

3) The heaviest rainfall rate occurs toward the upshear cloud edge, rather than the downshear edge.

The remainder of this section will concern case M2.

b. Estimation of latent heat release and liquid water mass for the model storm

In attempting to tie the model in with the preceding sections of this paper, it was desired to further check the apparent realism of the model storm by estimating its latent heat release and total liquid water mass. Accordingly, an attempt has been made here to do so by visualizing the plane of the model as a plane of symmetry and assuming a specific shape for the storm in horizontal planes normal to it. Note that with its rectangular geometry, the model is best regarded as simulating a vertical cross section of an infinitely long squall line, whereas previous estimates of latent heat release in actual severe storms have involved individual storms rather than squall lines. Therefore, for present purposes, the cloud outline in the two-dimensional model is re-interpreted as the vertical cross-section for a finite three-dimensional cloud, even though a fully three-dimensional model might have yielded considerably different point-by-point configurations and time dependencies.

For describing the method of estimation, we make use of symbols defined in Table 1. The following assumptions have been made:

1) Each hypothetical cloud slice lies in the x-y plane and is elliptical, with major axis intersecting the model plane (x-z) and minor axis one-half as long. The same assumption is made for precipitation regions. The assumed shape (Fig. 10) is reasonably well motivated by

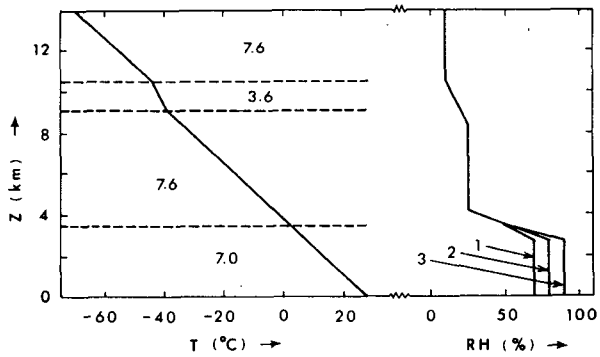

FIG. 7. Initial base states for air temperature T and relative humidity RH in the comparative experiments. Left: Numbers in the layers separated by dashed lines indicate the lapse rate $-\partial T/\partial z$ (°C km^{-1}) in each layer. Right: Cases 1, 2, and 3 refer to constant RH values of 70%, 80%, and 90% respectively, in the lowest 2.8 km.

satellite observations (for cirrus canopies generated by storms) and PPI radar echoes for sheared storms as in Fig. 2.

2) At each level, the horizontal average of a variable Q in the hypothetical three-dimensional cloud or precipitation region is the same as obtained from the two-dimensional model.

3) Mid-levels of the slices are at grid point levels, so that contributions from the lower ($j=1$) and upper ($j=N$) boundaries are weighted by half.

From the first assumption,

$$A_j=\pi n_j^2\Delta x^2/8 \tag{2}$$

and from the other two assumptions,

$$I_R(Q)\doteq\Delta z\sum_j \sigma_j A_j\tilde{Q}_j. \tag{3}$$

Equations (2) and (3) yield

$$I_R(Q)\doteq(\pi\Delta x^2\Delta z/8)\sum_j[\sigma_j n_j(\sum_i Q_{i,j})]. \tag{4}$$

In estimating either latent heat release or total liquid water mass (precipitation plus cloud droplets), R was taken to be the region of saturation C. In estimating total precipitation mass, R was taken to be the precipitation region P. By the method used for treating precipitation, P in this model was always within C. Throughout the 63-min time interval considered here, each slice for either P or C occurred in consecutive grid points, without "holes" (a small secondary cloud appearing late in the period was not counted).

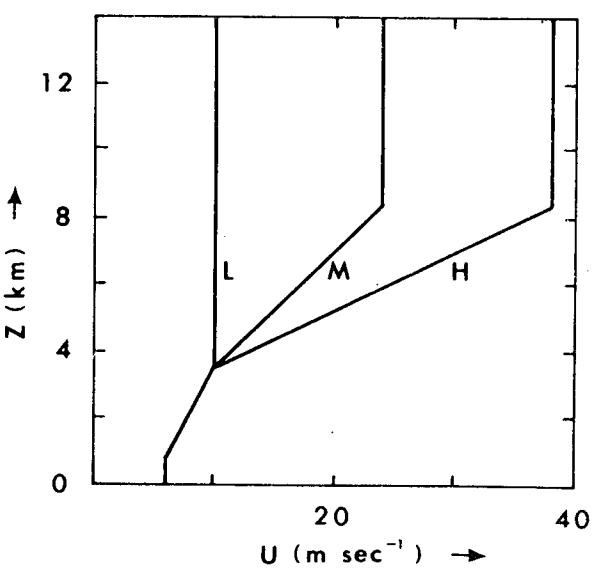

FIG. 8. Initial base states for the horizontal wind velocity in the comparative experiments. Cases L, M and H denote no shear, moderate shear, and strong shear respectively between 3.5 and 8.4 km.

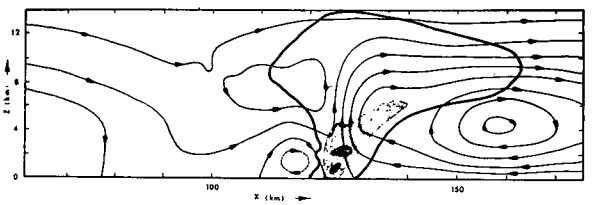

FIG. 9. Airflow streamlines relative to the moving cloud core and rain fall pattern for case M2 at 50 min. About two-thirds of the full grid length is shown, horizontal distance being measured from the initial left boundary. The heavy solid curve represents the cloud edge. Thinner solid curves with arrows are streamlines at streamfunction intervals of 10^7 gm m^{-1} sec^{-1}. Light and heavy shading represent rainfall rates of at least 30 and 90 mm hr^{-1} respectively. All later figures also refer to case M2.

The integrands Q representing the various properties per unit volume were as follows:

Latent heat release $\rho c_p(\gamma_d-\gamma_m)w$
Mass of liquid water L
Mass of precipitation L_p.

c. Results

For the model experiment, the perturbation circulation and liquid water distribution for a fixed subregion of the grid domain (108.8 km long) are shown in Fig. 11 for three stages of cloud development. At 18.5 min (Fig. 11a), the cloud is in its precipitation-free or "cumulus" stage; precipitation aloft commences around 22 min as the cloud top first penetrates the −20C level, following the parameterization of Takeda (1966). Near the beginning of the mature stage, at 36.1 min (Fig. 11b), precipitation has nearly reached the ground; toward the height of the mature stage, at 54.4 min (Fig. 11), anvil development is notable and there is heavy surface precipitation.

TABLE 1. List of symbols.

ρ	air density
c_p	specific heat at constant pressure for air (1.004×10^3 m^2 sec^{-2} °C^{-1})
γ_d	dry-adiabatic lapse rate (9.77×10^{-3} °C m^{-1})
γ_m	moist-adiabatic lapse rate
w	vertical velocity of air
L	liquid water content
L_p	precipitation content
i	horizontal grid index ($1\leq i\leq M$)
j	vertical grid index ($1\leq j\leq N$)
Q	unspecified variable
n_j	number of consecutive grid points at the jth grid level across a region of cloud or precipitation
Δx	horizontal grid separation
Δz	vertical grid separation
A_j	assumed horizontal cross-sectional area for cloud or precipitation slice at jth level
R	unspecified region
$I_R(Q)$	$\int\int\int Q\,dz\,dy\,dx$
$\tilde{Q}_j$	$(1/n_j)\sum_i Q_{i,j}$ where i sweeps across a region of cloud or precipitation within the grid
σ_j	weighting factors ($\frac{1}{2}$ for $j=1$ and $j=N$, 1 otherwise)

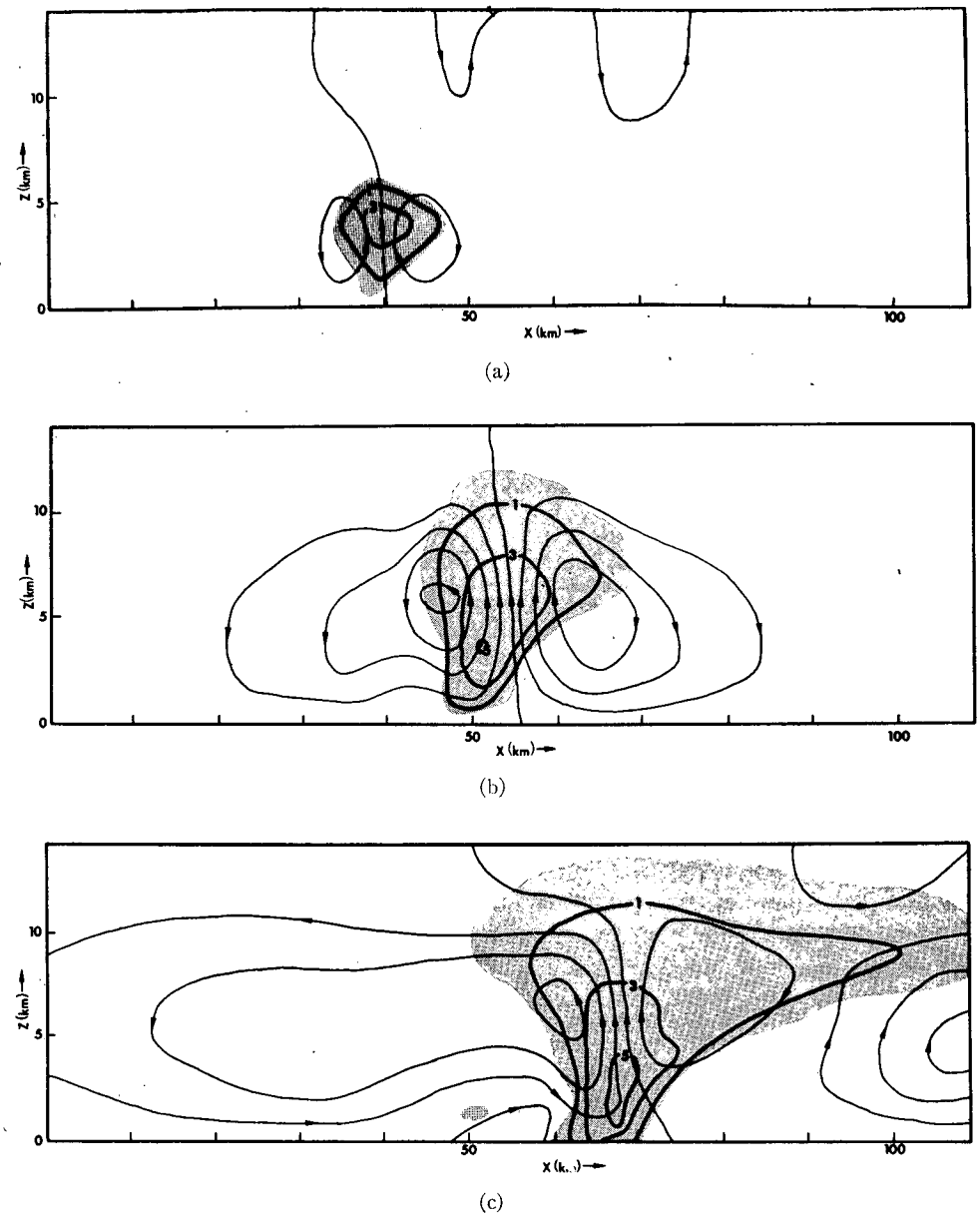

FIG. 11. Convection in a fixed subregion of the grid domain (see text) at: (a) 18.5 min, (b) 36.1 min, (c) 54.4 min. Horizontal distance is measured from the left boundary of the subregion. The cloud is indicated by shading. Thin solid curves with arrows are streamlines for the deviation of the flow from the base state, and are contoured at streamfunction intervals of 10^7 gm m^{-1} sec^{-1}. Thick solid curves are isolines of liquid water content L(gm m^{-3}).

Note that a direct comparison cannot be made between the isolines of liquid water content for the model (Fig. 11) and the actual RHI reflectivity contours in Fig. 2, since the model plane is along the mean flow while the RHI sections are across the mean flow. However, during the mature stage, the 1 gm m^{-3} isoline (Fig. 11c) does exhibit a shape grossly similar to that of RHI echoes along the mean flow for two mature "supercell" storms in Wokingham, England, and Geary, Okla. (Browning and Donaldson, 1963); the overall outline is noticeably asymmetric, spreading mainly downshear at upper levels, but the storm core stands nearly erect, as revealed by the axis of maximum liquid water content, despite midtropospheric ambient shear of roughly 3×10^{-3} sec^{-1}.

In the model cloud, as evident from Fig. 11, release of latent heat greatly dominates evaporative cooling. The maximum updraft velocities in the cloud core in Figs. 11a–11c are about 6, 11, and 10 m sec^{-1} respectively, while the downdraft near the upshear cloud edge

in Fig. 11c is only about 2.5 m sec^{-1}. This relatively weak downdraft development is apparently due to the highly simplified treatment of precipitation in the model; if rain had been allowed to fall into dry air outside the cloud without instantaneous total evaporation, or if hailfall and the cooling due to partial melting had been included, stronger downdraft development might have resulted.

Fig. 12 shows the time variation of latent heat release for the model storm. The graph indicates an initial rate of about 2×10^{11} cal sec^{-1} and slow development during the cumulus stage, followed by rapid intensification from around 20 min (just before the onset of precipitation) until about 35 min, then evolving to a much slower increase that continues through the remainder of the time interval. During the mature stage, the latent heat release is roughly 2.5×10^{12} cal sec^{-1}, similar to the average values near 3.5×10^{12} cal sec^{-1} estimated for the Oklahoma storm during the period 1840 through 1930 CST. The model estimate also compares favorably with values of 10^{12} to 10^{13} cal sec^{-1} estimated from geostationary satellite observations of individual severe storms occurring on 23 April 1968 in the east central United States (Sikdar *et al.*, 1970).

For completeness, it should be noted that the latent heat release plotted in Fig. 12 has been computed using horizontal averages which include weak downdrafts, with moist-adiabatic evaporation, as well as the main updraft with its condensation. Thus, referring to (1), the quantity plotted corresponds to G-E, rather than G

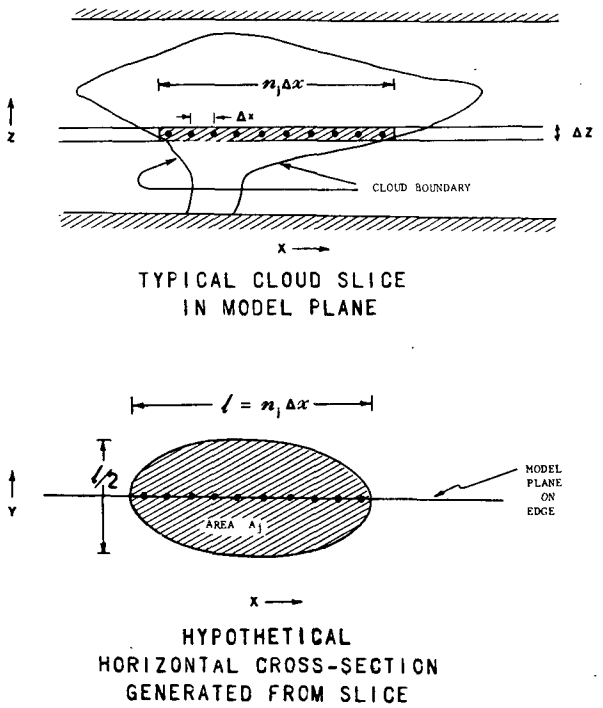

FIG. 10. Construction of hypothetical cross-sections for estimating mass-integrated quantities from the two-dimensional numerical model.

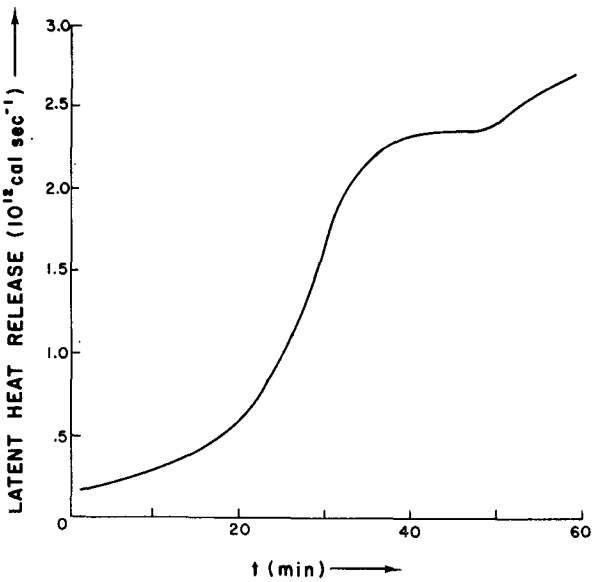

FIG. 12. Time variation of latent heat release estimated from the numerical model.

alone. However, since vertical motions in the model cloud are dominated by the main updraft, as is apparent from Fig. 11, order of magnitude comparisons remain valid within the limitations of the assumptions underlying the estimation method.

In Fig. 13, the masses for both precipitation and total liquid water are plotted. Since some liquid water drops detectable by radar may be insufficiently large to have significant relative fall speeds, the radar-detectable liquid water corresponding to the model storm might be thought of as being somewhere between the two amounts graphed. The slow increase of the latent heat release after 35 min has no counterpart in the total liquid water mass, which continues to increase rapidly; as of 63 min, its value is 1.3×10^{10} kg, which is at least an order of magnitude higher than the maximum radar-detectable liquid water for the Oklahoma storm in Fig. 5. The rapid increase reflects mainly the nearly linear growth of the anvil, which would go undetected by a radar. In the model storm, about 2×10^{8} kg of precipitation forms instantaneously near 22 min. The precipitation mass increases throughout the remainder of the time interval shown, but much more slowly than the total liquid water mass during maturity. At the end of the interval, the model storm contains about 3×10^{9} kg of precipitation. The radar-detectable liquid water content for the Oklahoma storm shows a maximum of 5.7 $\times10^{8}$ kg at the peak intensity of the storm. The closer similarity of estimated latent heat release rates between the observed storm and the model should not be regarded as merely fortuitous, because the storms approximate each other in overall dimensions, and such magnitudes of latent heat release have been calculated for thunderstorms from geostationary satellite data (Sikdar *et al.*, 1970).

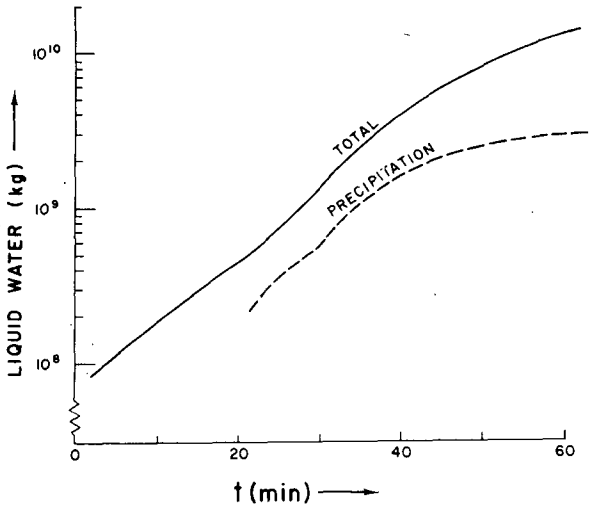

FIG. 13. Time variations of total liquid water content and precipitation content estimated from the numerical model.

It is only fair to note that the treatment of water substance in the numerical model, as described previously (Schlesinger, 1973), leads to some admittedly unrealistic features. Precipitation is everywhere accompanied by 1 gm m^{-3} of cloud droplets, with saturated air, and cannot fall out of the cloud base without completely evaporating. (As noted earlier, this limitation may partly explain the weak development of the model downdraft.) Surface rainfall is preceded by descent of the cloud base to the ground. This is in contrast to actual thunderstorms, which commonly feature a well-defined cloud base from which heavy precipitation may reach the ground without saturating the air, perhaps even accompanied by a decrease in surface relative humidity (Byers and Braham, 1949). The omission of the ice phase latent heat is not regarded as a primary drawback in the present context, since the same simplifying assumption was made in estimating parameters in the Oklahoma storm. However, this neglected energy ($\sim$80 cal gm^{-1}) is about 13% of the latent heat of condensation ($\sim$600 cal gm^{-1}), and could appreciably increase buoyancy in the upper parts of the cloud.

As already noted, the extension to elliptical horizontal cloud layers from plane cross-sections departs from the rectilinear geometry of the model, originally designed for simulating roll-type convection. In this context, the estimates of latent heat release and liquid water content presented here should be regarded cautiously, in light of recent numerical cloud modeling results obtained by Soong and Ogura (1973) and Murray (1970).

In these cases, two experiments were run, one using axial symmetry and the other using slab symmetry. Both geometries used identical base states, initial perturbations, governing equations and boundary conditions. Soong and Ogura, as well as Murray, found that the axially symmetric cloud developed more vigorously than the slab-symmetric cloud. A stronger updraft, and in turn more liquid water production, resulted. Along the axis of symmetry, the maximum rainwater content in the precipitating model of Soong and Ogura was about half as great for the slab-symmetric cloud; the corresponding ratio for cloud water in Murray's nonprecipitating model was only about 1:4. Maximum updraft velocities showed similar contrasts.

This suggests that the estimates of cloud-integrated liquid water content and latent heat release in the model storm might be conservative, since they are generated from a rectilinear two-dimensional model and the cylindrical geometry better approximates three-dimensionality then the rectilinear geometry. However, the areal proportion of a horizontal cloud slice occupied by the active core is larger in the rectilinear geometry than in the cylindrical geometry, thereby weighting the core contributions to horizontal averages more strongly. Hence, assuming equal horizontal averages for a rectangular model cloud slice and for the elliptical wafer generated from it should tend to counteract the tendency of a relatively weak storm core to limit the magnitudes of the integrals involved.

The smooth time variations in Figs. 12 and 13 should be contrasted with the more irregular variations shown in Figs. 3 and 5 for the Oklahoma storm. Computationally produced pseudo-diffusion (Schlesinger, 1973) may be partly responsible. Also, the omission of the ice phase precludes hail. Nevertheless, the magnitudes of the estimated latent heat release and liquid water content in the model storm appear to uphold the apparent ability of the model to reasonably simulate "supercell" storms as suggested by the earlier results which have been reviewed.

6. Concluding remarks

In this paper, the time variation of mass-integrated liquid water content and latent heat release for a severe thunderstorm in pronounced vertical shear has been investigated in two phases. An actual storm in Oklahoma has been analyzed, and the observed magnitudes have then been compared with those estimated from a previous two-dimensional numerical modeling experiment (Schlesinger, 1973).

1) For the Oklahoma storm, both latent heat release and radar-detectable liquid water content are found to maintain the same order of magnitude during maturity, despite fluctuations apparently associated with a funnel cloud and surface hail. Latent heat release ranges between about 2 and 8×10^{12} cal sec^{-1}, while liquid water mass is between 1 and 5×10^{8} kg.

2) Both the liquid water mass and the latent heat release are at least an order of magnitude greater for the Oklahoma storm than the values estimated for air-mass thunderstorms by Braham (1952).

3) From an initial value near 2×10^{11} cal sec^{-1}, latent heat release in the model storm increases to about 2.5×10^{12} cal sec^{-1} by 35 min and is then steady or only

slightly increasing through 63 min. Total liquid water mass increases by an order of magnitude during this mature phase, nearly as rapidly as in the preceding 35 min, reaching slightly more than 10^{10} kg at the end of the interval. Precipitation content, presumably a closer analogue of radar-detectable liquid water, increases considerably more slowly during maturity and shows signs of leveling off near 3×10^9 kg.

4) Thus, in the mature phase, both the actual storm and the model storm exhibit comparable values for latent heat release as well as radar-detectable liquid water, identifying the latter with precipitation particles. Omission of the ice phase from consideration in both analyses is presumably not a major error, since the heat of vaporization is about 7.5 times the heat of fusion.

Acknowledgments. The preliminary research reported in this paper was performed in phase I of the continuing studies on energetics of hail storms supported by the National Science Foundation under NSF grant GI-31278X. The courtesy of Mr. J. T. Dooley of the National Severe Storms Laboratory in supplying the observational data used in this study is much appreciated. We wish to thank Dr. Chester W. Newton for numerous suggestions on improving the manuscript. Thanks are also due to Gary Ellrod and Sanjay Limaye for computing some of the data reported in this paper.

REFERENCES

Barge, B., 1968: Thunderstorm energy budgets from radar. Proc. 13th Radar Meteor. Conf., Amer. Meteor. Soc., Boston, Mass., 114–117.

Barnes, S. L., J. H. Henderson, and R. J. Ketchum, 1971: Rawinsonde observation and processing techniques at the NSSL. NOAA Technical Memo ERL NSSL-53, Norman, Okla., 246 pp.

Braham, R., 1952: The water and energy budgets of the thunderstorm and their relation to thunderstorm development. *J. Meteor.*, **9**, 227–242.

Brown, R. A., 1967: Mass and available energy in growing convective clouds. *J. Atmos. Sci.*, **24**, 308–311.

Browning, K. A., and R. J. Donaldson, 1963: Airflow and structure of a tornadic storm. *J. Atmos. Sci.*, **20**, 533–545.

——, and F. H. Ludlam, 1962: Airflow in convective storms. *Quart. J. Roy. Meteor. Soc.*, **88**, 117–135.

Byers, H., and R. R. Braham, Jr., 1949: *The Thunderstorm.* U. S. Govt. Printing Office, Washington, D. C., 287 pp.

Ellrod, G. P., 1973: Time variation of latent heat release during the evolution of Oklahoma thunderstorms as estimated from radar observations. M.S. Thesis, University of Wisconsin, 44 pp.

Fankhauser, J. C., 1971: Thunderstorm-environment interactions determined from aircraft and radar observations. *Mon. Wea. Rev.*, **99**, 171–192.

Fawbush, E. J., and R. C. Miller, 1953: A method for forecasting hailstone size at the earth's surface. *Bull. Amer. Meteor. Soc.*, **34**, 235–244.

Geotis, S. G., 1971: Thunderstorm water contents and rain fluxe deduced from radar. *J. Appl. Meteor.*, **10**, 1233–1237.

Gunn, K. L. S., and J. S. Marshall, 1958: The distribution with size of aggregate snowflakes. *J. Meteor.*, **15**, 452–461.

Holtz, C. D., 1968: Life cycle of a summer storm from radar records. Report #MW-55, McGill University, Montreal, Canada, 46 pp.

Ludlam, F. H., 1963: Severe local storms—a review. *Meteor. Monogr.*, **5**, No. 27, 1–30.

Marwitz, J. D., 1972: The structure and motion of severe hailstorms. Part I: Supercell storms. *J. Appl. Meteor.*, **11**, 166–179.

McLaughlin, M. R., 1967: The energy budget of a severe local storm. Report #7, University of Texas, Austin, Tex., 55 pp.

Murray, F. W., 1970: Numerical models of a tropical cumulus cloud with bilateral and axial symmetry. *Mon. Wea. Rev.*, **98**, 14–28.

Schlesinger, R. E., 1973: A numerical model of deep moist convection: Part I. Comparative experiments for variable ambient moisture and wind shear. *J. Atmos. Sci.*, **30**, 835–856.

Sikdar, D. N., V. E. Suomi, and C. E. Anderson, 1970: Convective transport of mass and energy in severe storms over the United States—an estimate from a geostationary altitude. *Tellus*, **22**, 521–532.

Soong, S., and Y. Ogura, 1973: A comparison between axisymmetric and slab-symmetric cumulus cloud models. *J. Atmos. Sci.*, **30**, 879–893.

Takeda, T., 1966: Effects of the prevailing wind with vertical shear on the convective cloud accompanied with heavy rainfall. *J. Meteor. Soc. Japan*, **44**, 129–143.

U. S. Department of Commerce, 1968: *Storm Data*, **10**, No. 5, Environmental Sciences Service Administration, Environmental Data Service.

Wilson, J. W., 1969: Radar measurements of rainfall for operational purposes. Final Report 7488-360 on Contract E 22-23-69(N), Hartford, Conn., 44 pp.